Supplementary Information for

Ultrafast-charging and durable organic cathodes enabled by two-dimensional supramolecular engineering

Li Liu, Xianming Deng, Qingxuan Chen, Yuantao Ma, Xinming Zhang, Hongyin Hu, Ling Qiu, Lele Peng* and Zhen Chen*

* Correspondence: penglele@sz.tsinghua.edu.cn (L.P.); zhen.chen@sz.tsinghua.edu.cn (Z.C.)

This PDF file includes:

1. Supplementary Notes 1−3
2. Supplementary Figures 1−30
3. Supplementary Tables 1−5
4. Supplementary References 1−30

1. Supplementary Notes

Supplementary Note 1 | Kinetic analysis of Li^+ storage

The electrochemical reaction kinetics was investigated through cyclic voltammetry measurements. Theoretically, the current (i) response to the applied scan rate (v) follows the equation (S1) as below,

$$i = a \cdot v^b \tag{S1}$$

, where b refers to the slope of the linear fit of the log-log plot. According to the power law described above, a redox reaction limited by semi-infinite linear diffusion gives a b value of 0.5, while for a surface-controlled capacitive process, the b value is close to 1.0. Furthermore, the capacitive ($k_1 \cdot v$) and diffusive ($k_2 \cdot v^{1/2}$) contributions were further quantified according to the equation (S2),

$$i = k_1 \cdot v + k_2 \cdot v^{1/2} \tag{S2}$$

, where k_1 and k_2 constants can be obtained by plotting $i \cdot v^{-1/2}$ against $v^{1/2}$.

Supplementary Note 2 | Determination of Li^+ diffusion coefficients

In the Nyquist plots, the linear part of the Warburg impedance is directly related to Li^+ diffusion in the cathode materials. The D_{Li^+} values were also calculated based on the equation (S3):

$$D_{Li^+} = \frac{1}{2}\left(\frac{RT}{ACn^2F^2\sigma_w}\right)^2 \tag{S3}$$

, where R is the gas constant, T is the room temperature (298 K), A represents the surface area of electrode, C is the concentration of Li^+, n is the number of transferred electrons, F is the Faraday constant, and σ_w denotes the slope obtained by the linear fitting of the real part (Z') of impedance and low frequency (ω) according to the equation (S4),

$$Z' = R_s + R_{sei} + R_{ct} + \sigma_w \cdot \omega^{-1/2} \tag{S4}$$

, where R_s, R_{sei}, and R_{ct} is the resistance of the electrolyte, the Li^+ migration through SEI and the desolvation process, respectively.

Supplementary Note 3 | Determination of activation energies

To determine the activation energies during Li^+ desolvation and diffusion, respectively, the important parameters for Li^+ transport kinetics represented by the charge transfer resistance (R_{ct}) and D_{Li^+} were measured by temperature-dependent EIS from 30 to −30 °C. According to the classic Arrhenius law, the R_{ct} and D_{Li^+} values at varying temperatures were fitted into the equations (S5) and (S6), respectively,

$$\ln R_{ct}^{-1} = \ln A - \frac{E_{a,ct}}{RT} \tag{S5}$$

$$\ln D_{Li^+} = \ln B - \frac{E_{a,D}}{RT} \quad \text{(S6)}$$

, where A and B are pre-exponential factors, R is the gas constant, T is the absolute temperature, $E_{a,ct}$ and $E_{a,D}$ are the activation energies for Li^+ desolvation and diffusion, respectively.

2. Supplementary Figures

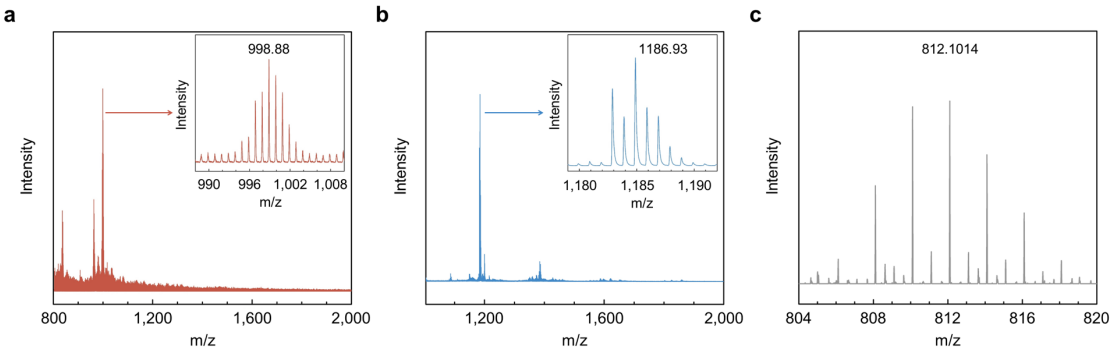

Supplementary Fig. 1 | Structure characterization of heterocyclic TTQs.
(a,b) MALDI-TOF mass spectra (positive mode): (a) STTQ-**1** and (b) STTQ-**2**. (c) High-resolution ESI mass spectrum (negative mode) of OTTQ.

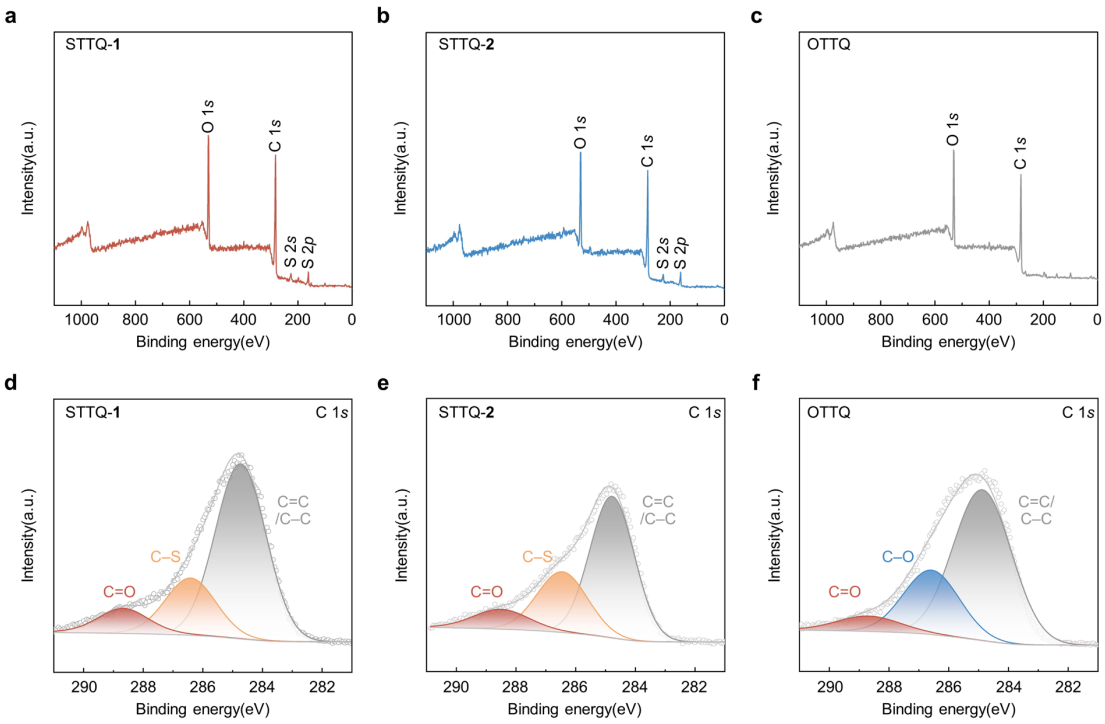

Supplementary Fig. 2 | Chemical characterization of heterocyclic TTQs.
XPS spectra of bulk samples: (a–c) Survey scans and (d–f) C 1*s* core-level spectra for STTQ-**1** (a,d), STTQ-**2** (b,e), and OTTQ (c,f).

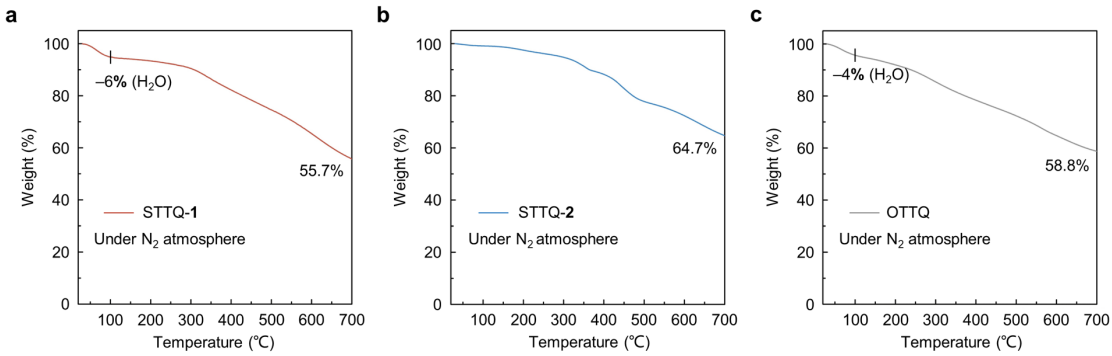

Supplementary Fig. 3 | Evaluation on the thermal stability of heterocyclic TTQs. TGA profiles of the powdery samples under nitrogen atmosphere: (a) STTQ-**1**, (b) STTQ-**2** and (c) OTTQ.

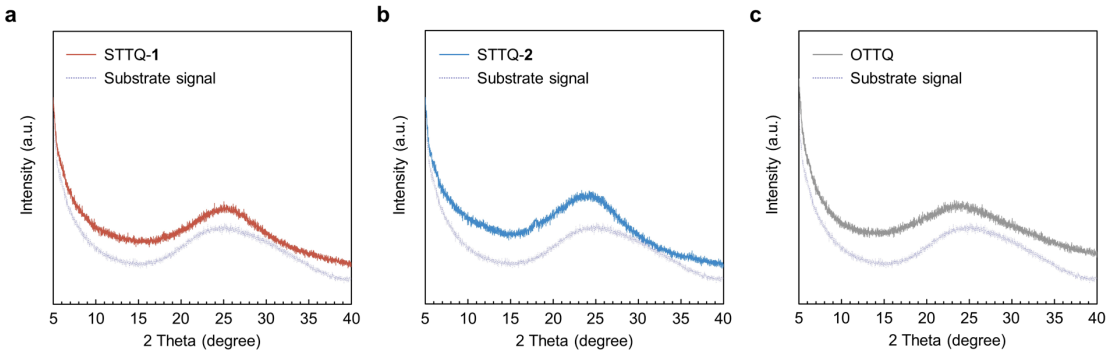

Supplementary Fig. 4 | Evaluation on the crystallinity of heterocyclic TTQs. XRD patterns of the powdery samples at 25 °C: (a) STTQ-**1**, (b) STTQ-**2** and (c) OTTQ. None of the distinct peaks can be observed in the XRD patterns.

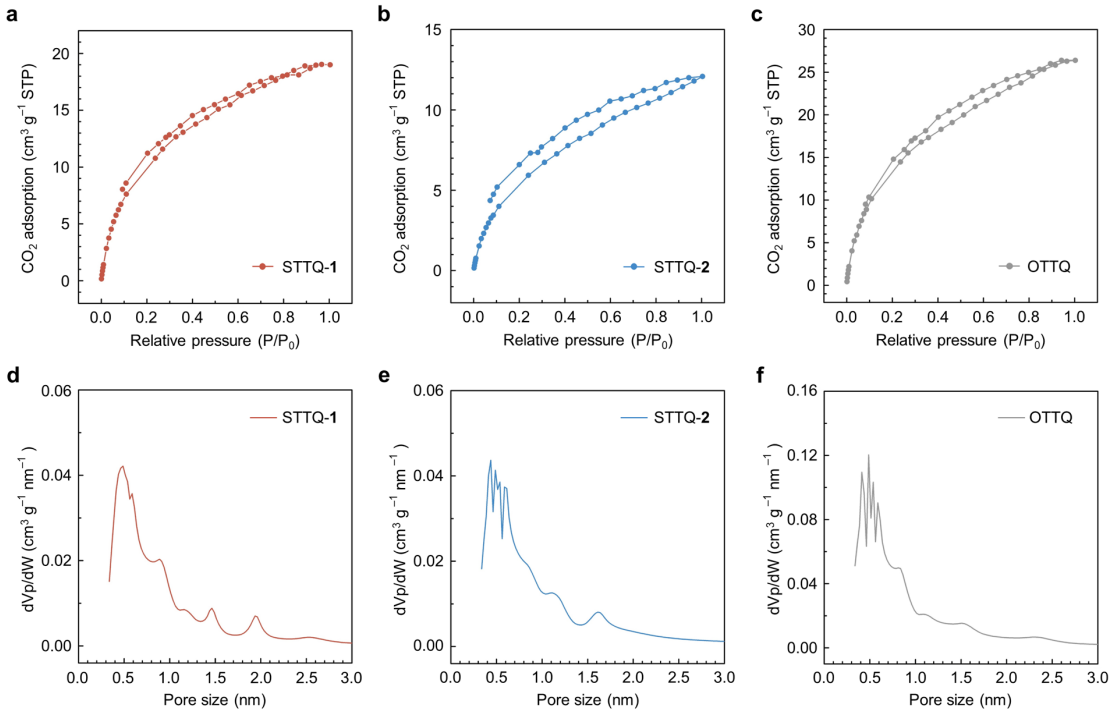

Supplementary Fig. 5 | Evaluation on the porosity of heterocyclic TTQs.
CO_2 adsorption-desorption isotherms (a–c) and pore size distribution curves (d–f): STTQ-**1** (a,d), STTQ-**2** (b,e), and OTTQ (c,f).

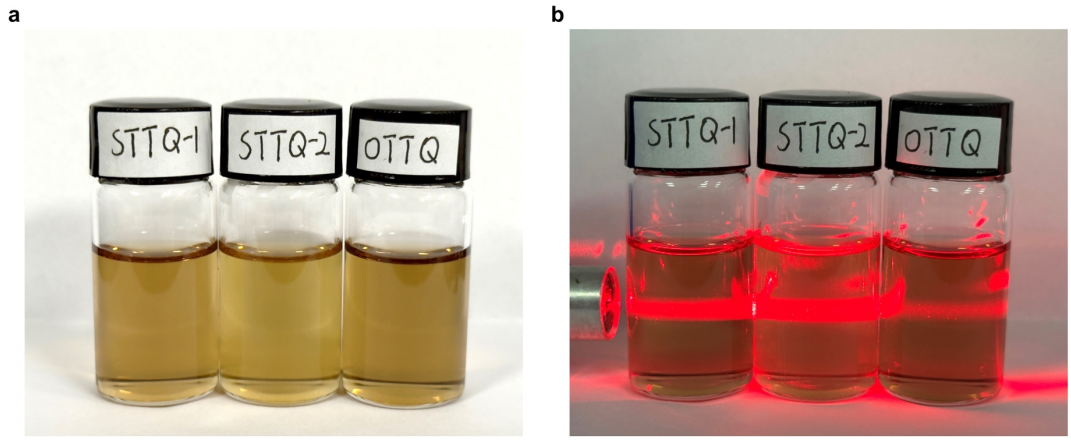

Supplementary Fig. 6 | Evaluation on the Tyndall effect of heterocyclic TTQ dispersions.

Photographs of the dispersions in DMF after ultrasonication at 25 °C: (a) without light scattering and (b) with light scattering by laser irradiation.

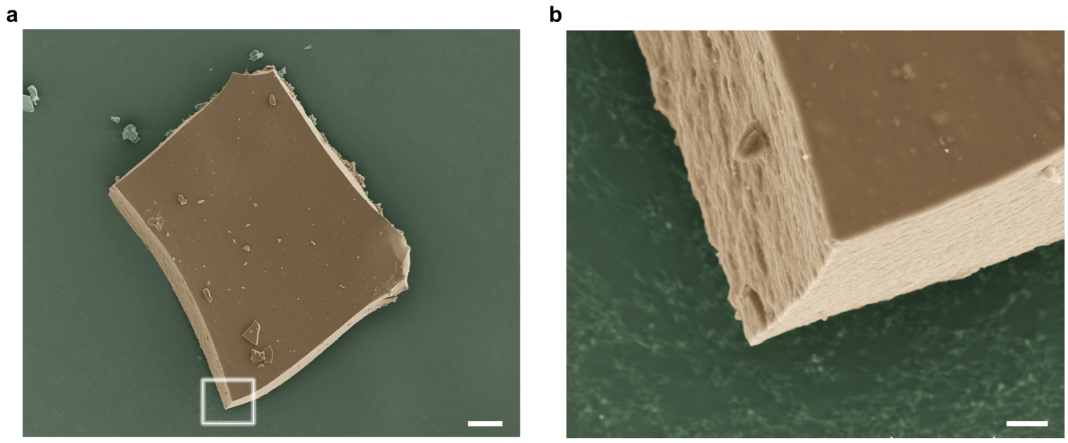

Supplementary Fig. 7 | Compact laminar structures of STTQ-1.
(a) Low-magnification overview. Scale bars, 20 μm. (b) High-magnification views of selected areas marked by white boxes in a. Scale bars, 2 μm.

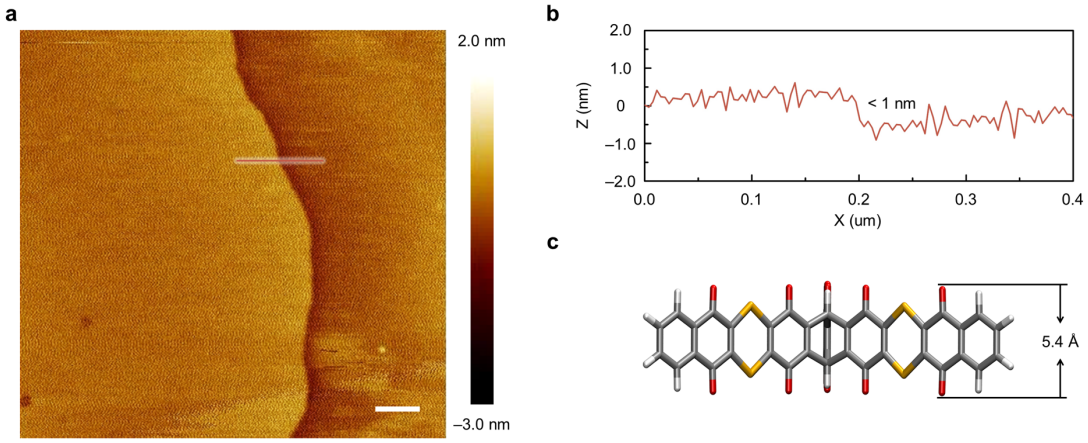

Supplementary Fig. 8 | Nanostructure characterization of STTQ-1 monolayer nanosheets.

Tapping-mode AFM topographical images (a) and height profiles (b) of the exfoliated monolayer nanosheets on mica substrates. Scale bar, 0.2 μm. (c) Sticks model of STTQ-**1** from side view.

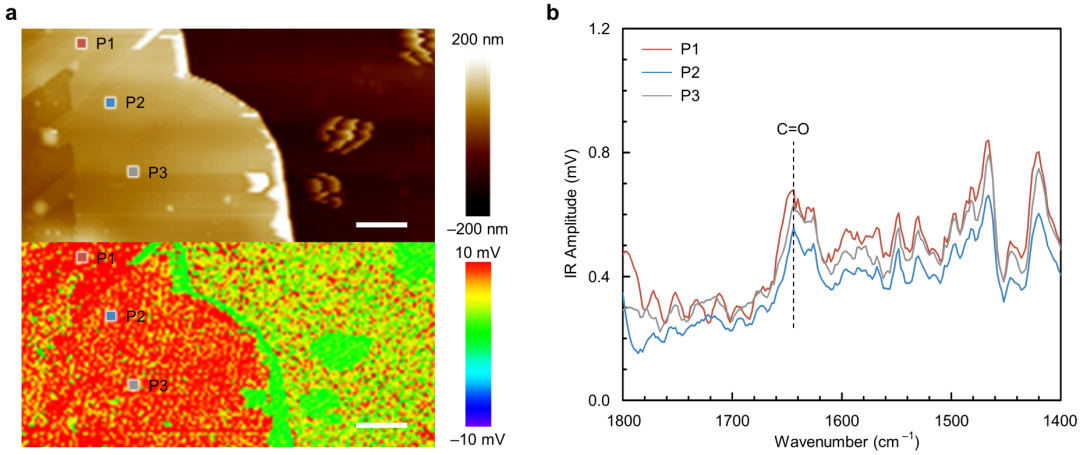

Supplementary Fig. 9 | Evaluation on the molecular orientation of the exfoliated STTQ-1 nanosheets.

(a) Tapping-mode AFM images (upper) and AFM-IR mapping at 1650 cm^{-1} (lower) on silicon substrate. Marked points (P1–P3) indicate spectral acquisition locations. Scale bars, 2 μm. (b) Corresponding AFM-IR spectra (1400–1800 cm^{-1}) from P1 (red), P2 (blue), P3 (gray) in a.

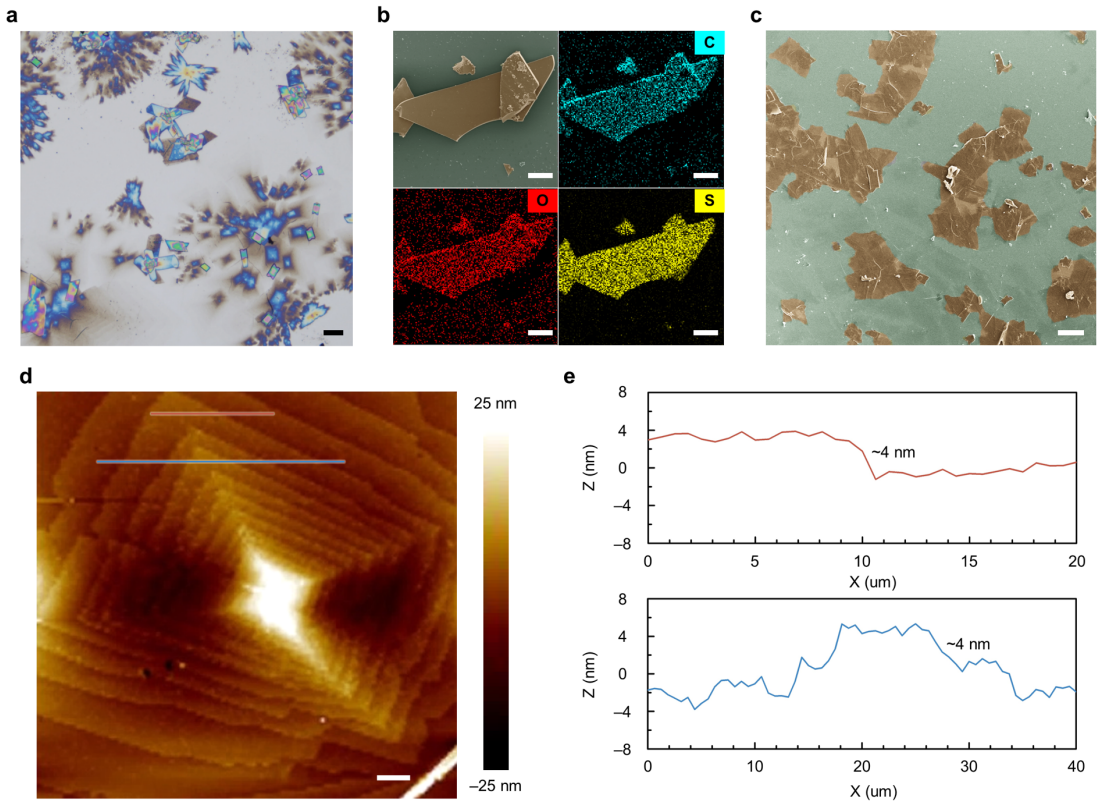

Supplementary Fig. 10 | Morphology characterization of STTQ-2.
(a) Reflection-mode OM image of a drop-casted sample on silicon. Scale bar, 20 μm. (b) False-colored SEM image and corresponding EDX elemental mapping of a drop-casted sample on silicon. Scale bars, 20 μm. (c) False-colored SEM image of exfoliated nanosheets on silicon. Scale bar, 20 μm. (d) Tapping-mode AFM image and (e) height profile of multilayer nanosheets on silicon. Scale bar, 5 μm.

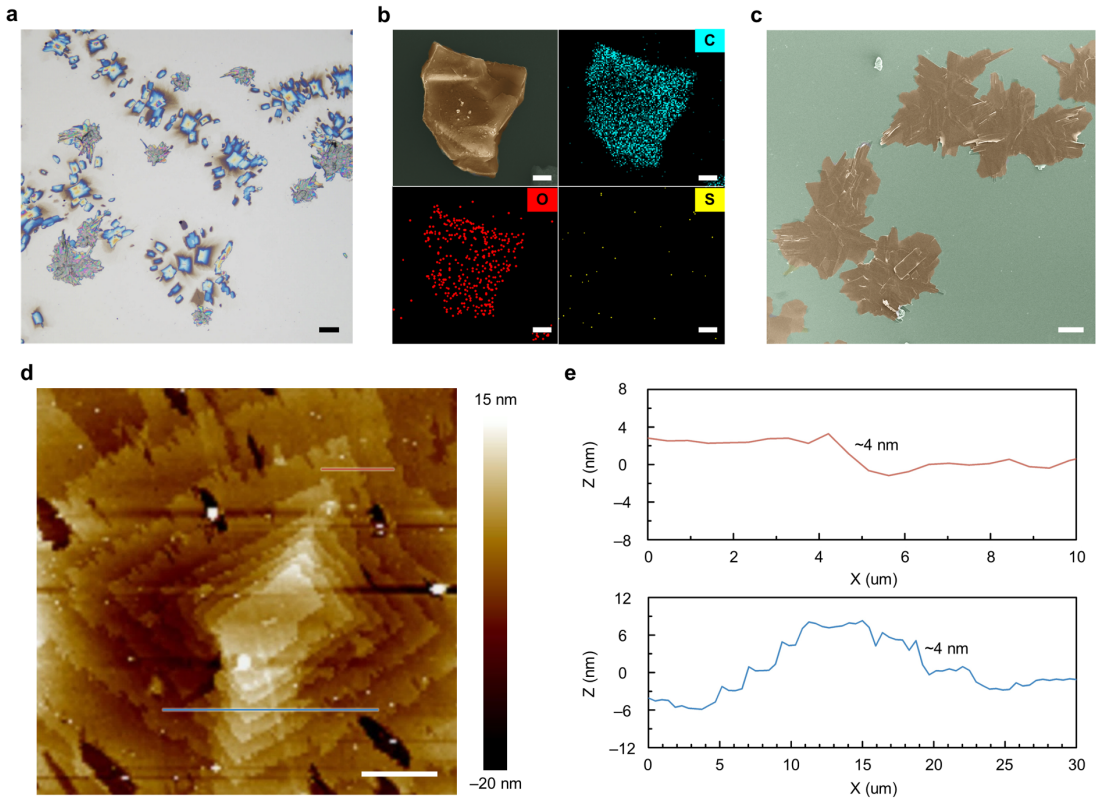

Supplementary Fig. 11 | Morphology characterization of OTTQ.
(a) Reflection-mode OM image of a drop-casted sample on silicon. Scale bar, 10 μm. (b) False-colored SEM image and corresponding EDX elemental mapping of a drop-casted sample on silicon. Scale bars, 10 μm. (c) False-colored SEM image of exfoliated nanosheets on silicon. Scale bar, 20 μm. (d) Tapping-mode AFM image and (e) height profile of multilayer nanosheets on silicon. Scale bar, 10 μm.

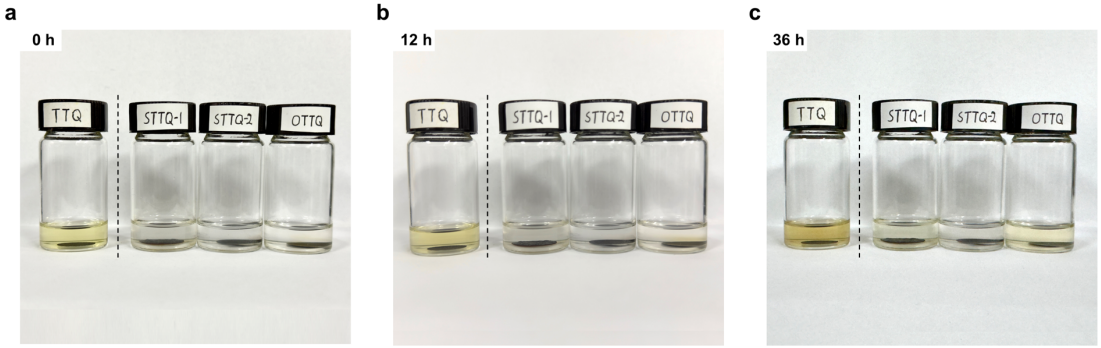

Supplementary Fig. 12 | Evaluation on the solubility of TTQ electrodes.
Photographs of TTQ and heterocyclic TTQs electrodes immersed in LiTFSI DOL/DME solution (1 M) observed after 0 h (a), 12 h (b), and 36 h (c). TTQ dissolved significantly with increasing immersion time, while the heterocyclic TTQs remained largely insoluble.

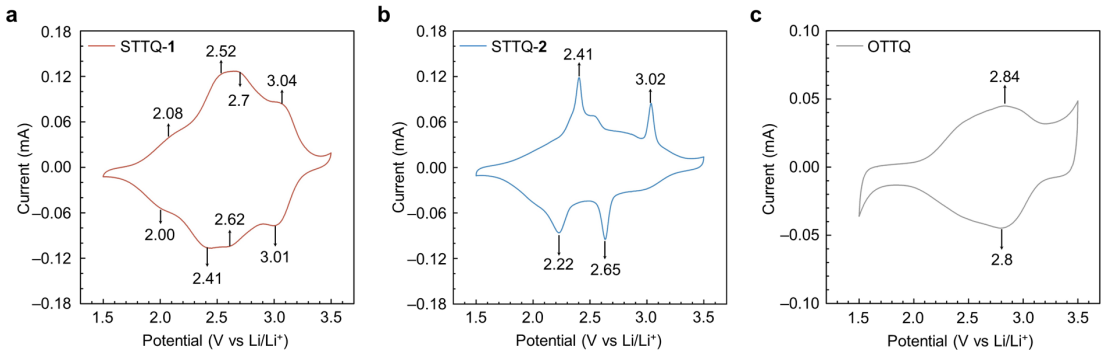

Supplementary Fig. 13 | Cyclic voltammetry (CV) curves of heterocyclic TTQs. CV curves at a scan rate of 0.5 mV s^{-1} with redox peak potentials labeled: (a) STTQ-**1**, (b) STTQ-**2**, and (c) OTTQ.

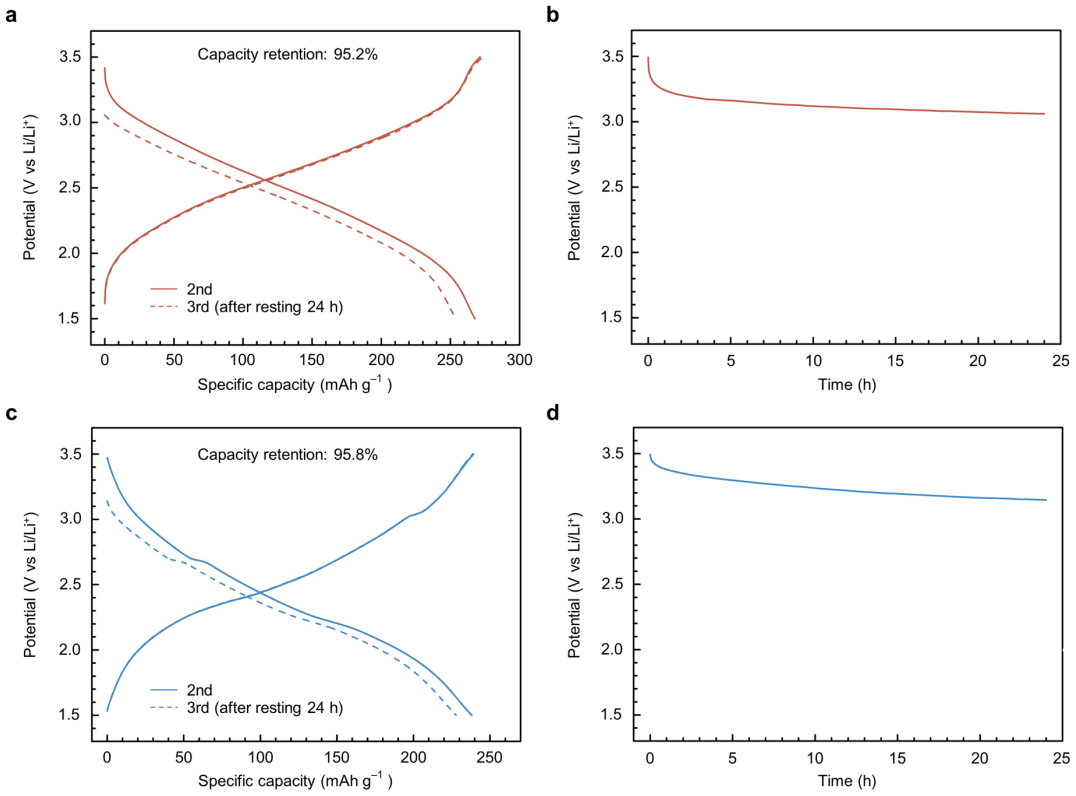

Supplementary Fig. 14 | Evaluation on the self-discharge properties of STTQ. Galvanostatic charge–discharge profiles (a,c) at a current density of 0.06 A g^{-1} and voltage evolution for 24 h (b,d) at the second and third cycles: (a,b) STTQ-**1** and (c,d) STTQ-**2**.

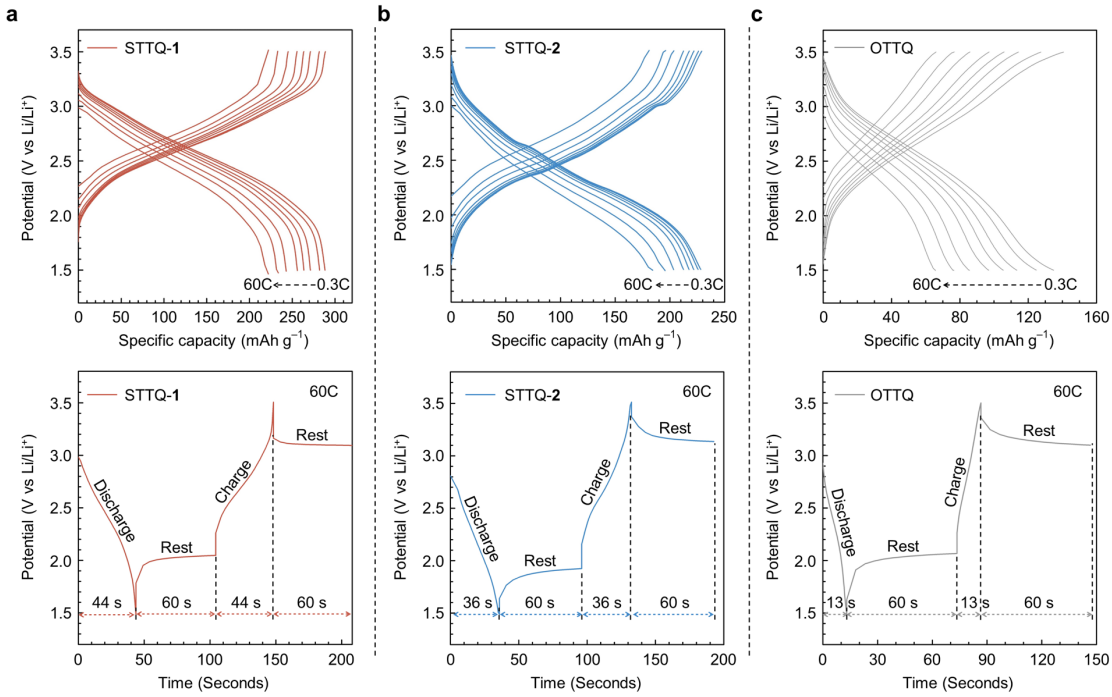

Supplementary Fig. 15 | Evaluation on the rate performance of heterocyclic TTQs. Galvanostatic charge–discharge profiles (upper) at 25 °C across rates from 0.3C to 60C and charge–discharge duration at 60C (lower): (a) STTQ-**1**, (b) STTQ-**2**, and (c) OTTQ.

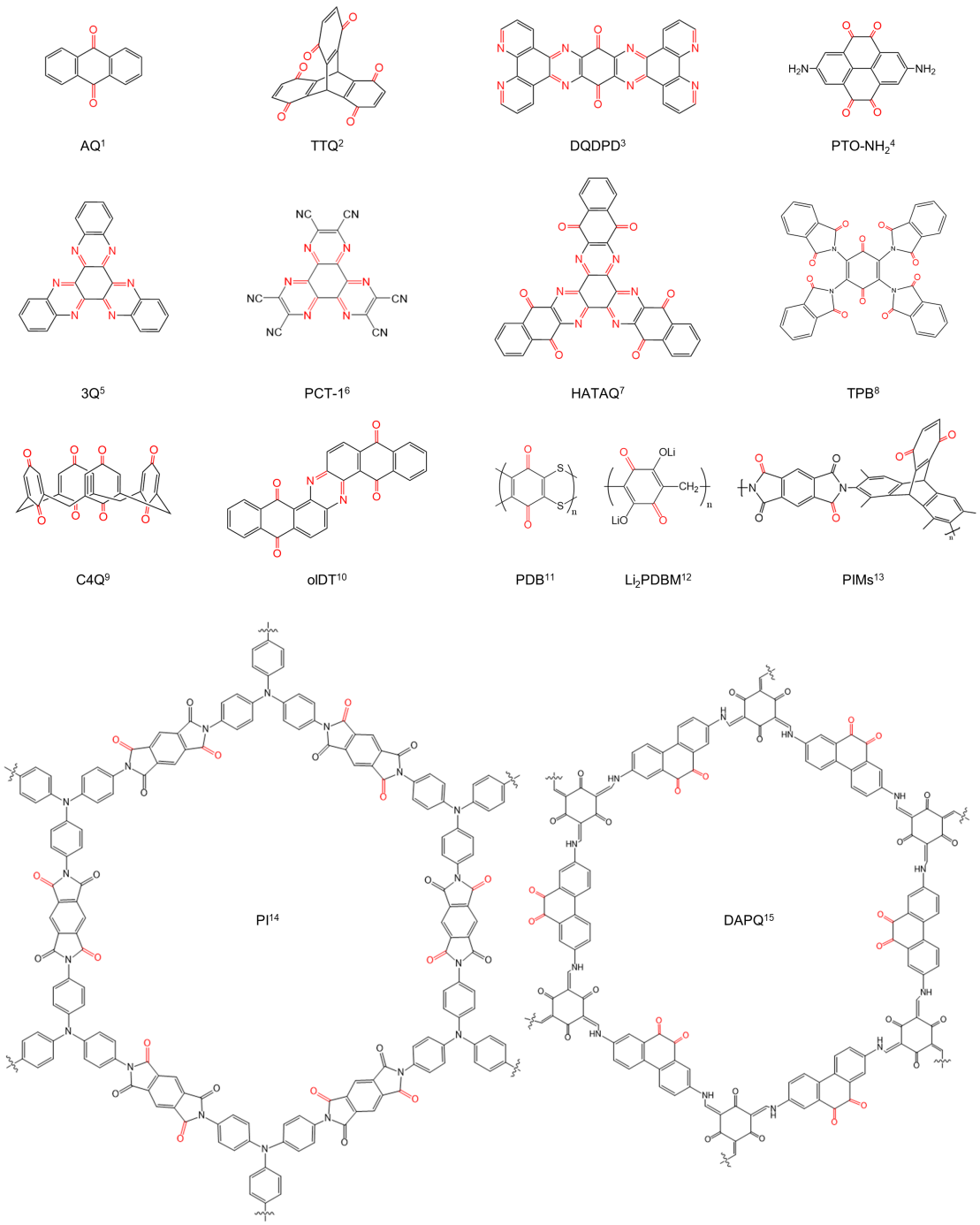

Supplementary Fig. 16 (Continued to the subsequent page) | Representative examples of organic cathode materials.

Molecular structures of redox-active organic materials reported in the literatures.[1-15]

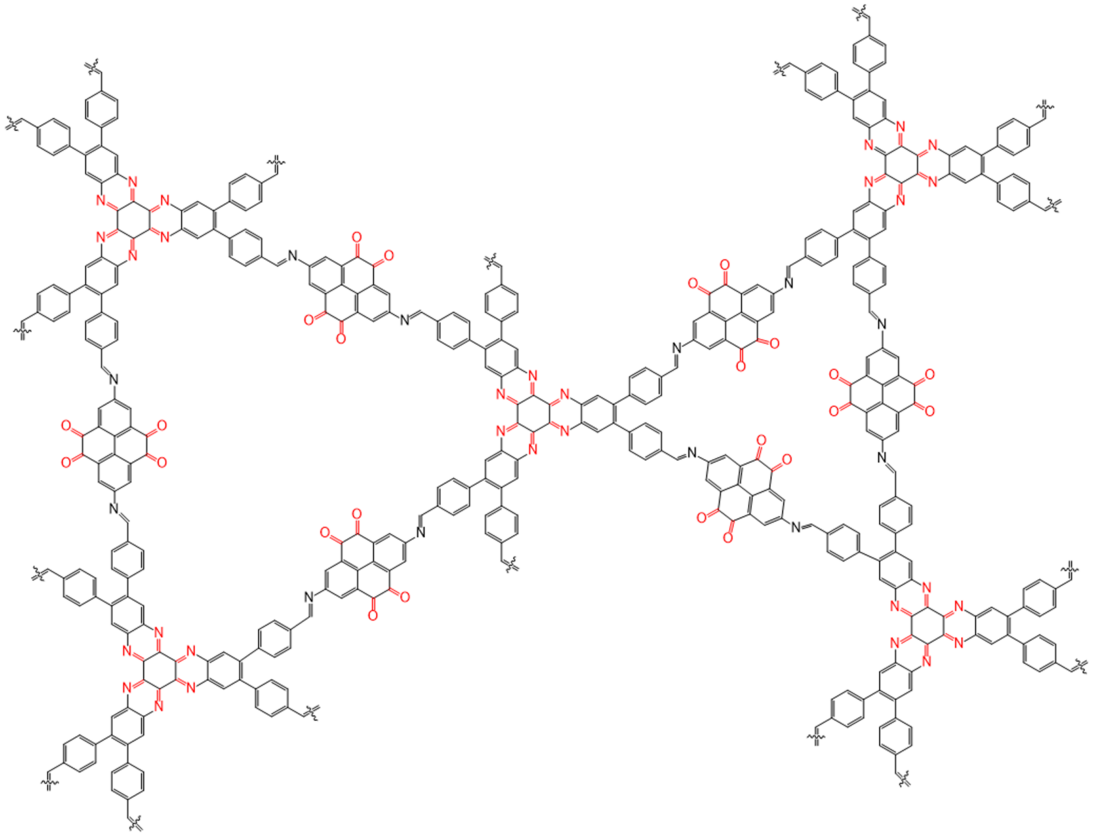

USTB[16]

Supplementary Fig. 16 (Followed with the front page) | Representative examples of organic cathode materials.

Molecular structures of redox-active organic materials reported in the literatures.[16]

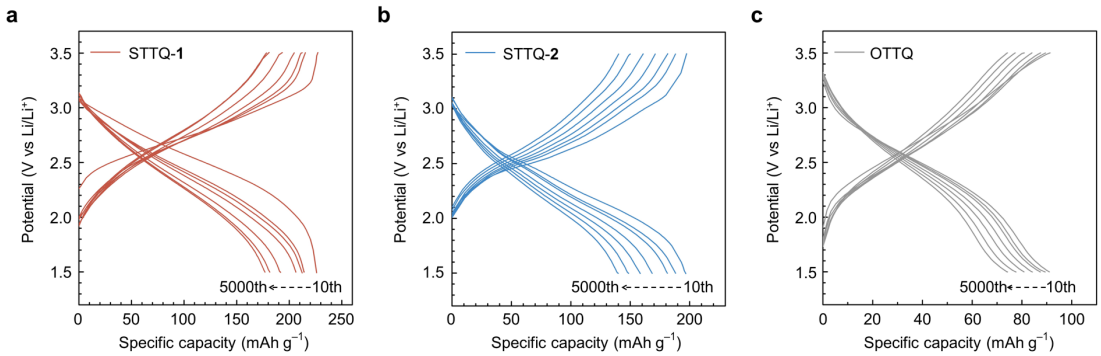

Supplementary Fig. 17 | Evaluation on the cycling performance of heterocyclic TTQs.

Galvanostatic charge–discharge profiles from the 10th to 5000th cycle at a current density of 4.5 A g^{-1} (15C): (a) STTQ-**1**, (b) STTQ-**2**, and (c) OTTQ.

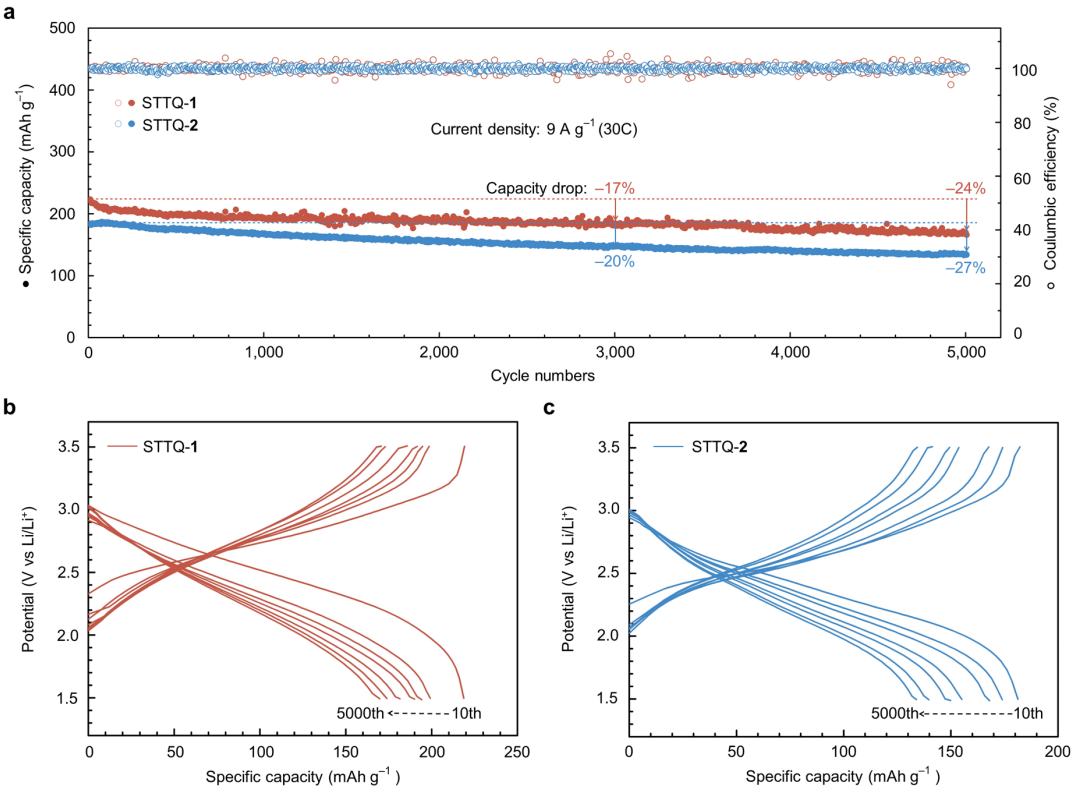

Supplementary Fig. 18 | Evaluation on the cycling performance of STTQs.
(a) Long-term cycling (dots) and coulombic efficiency (circles) of STTQ-**1** and STTQ-**2** at a current density of 9.0 A g^{-1} (30C). (b) Galvanostatic charge–discharge profiles of STTQ-**1** from the 10^{th} to 5000^{th} cycle at a current density of 9.0 A g^{-1} (30C). (c) Galvanostatic charge-discharge profiles of STTQ-**2** from the 10^{th} to 5000^{th} cycle at a current density of 9.0 A g^{-1} (30C).

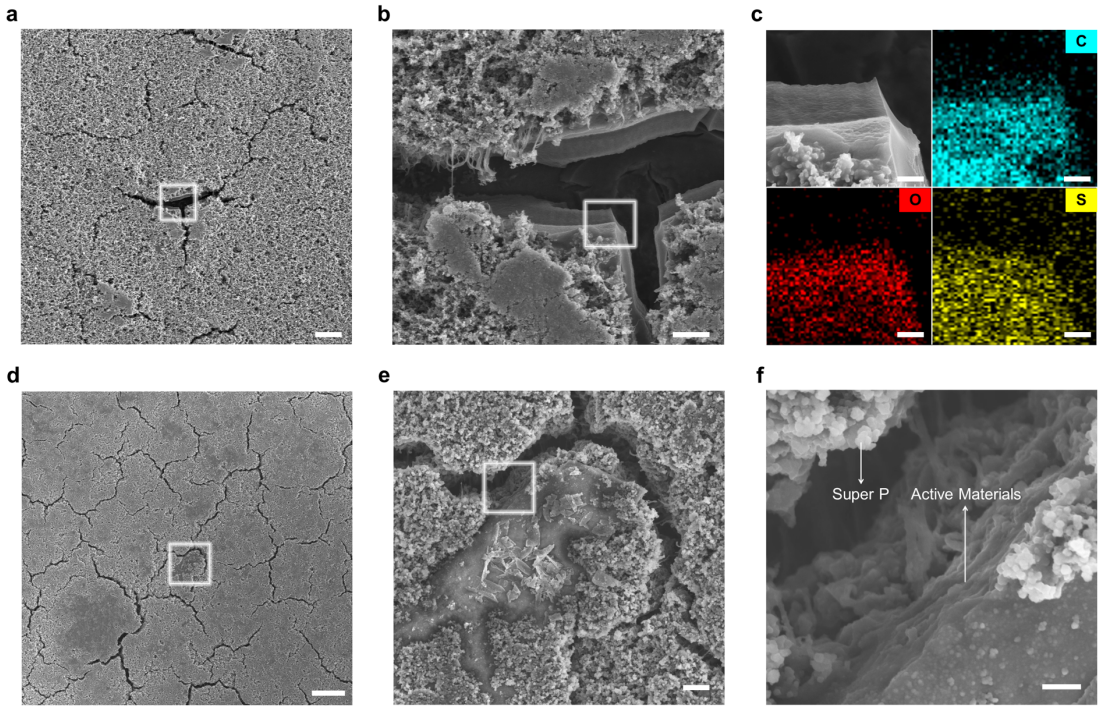

Supplementary Fig. 19 | Characterization of morphology evolution in the STTQ-1 cathode over 2000 cycles.

(a–c) Morphology before cycling: (a) Overview. Scale bar, 10 μm. (b) Enlarged view of the boxed region in a. Scale bar, 2 μm. (c) Further enlarged view of the boxed region in b with corresponding EDX elemental mapping of compact laminar structures. Scale bars, 0.5 μm. (d–f) Morphology after cycling: (d) Overview. Scale bar, 20 μm. (e) Enlarged view of the boxed region in d. Scale bar, 2 μm. (f) Further enlarged view of the boxed region in e. Scale bar, 0.5 μm.

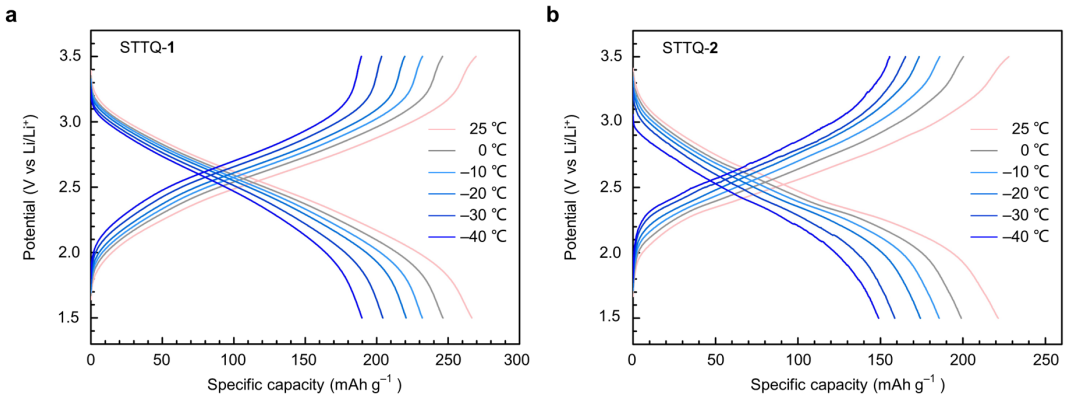

Supplementary Fig. 20 | Evaluation on the low-temperature performance of STTQs.

Galvanostatic charge–discharge profiles at different temperatures ranging from 25 to −40 °C: (a) STTQ-**1** and (b) STTQ-**2**.

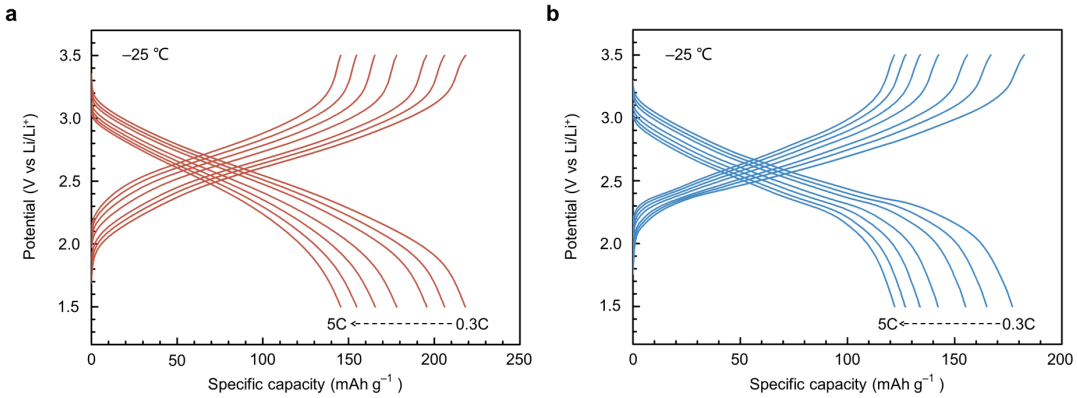

Supplementary Fig. 21 | Evaluation on the rate performance of STTQs at low temperature.

Galvanostatic charge–discharge profiles in a range of charge rates from 0.3C to 5C at −25 °C: (a) STTQ-**1** and (b) STTQ-**2**.

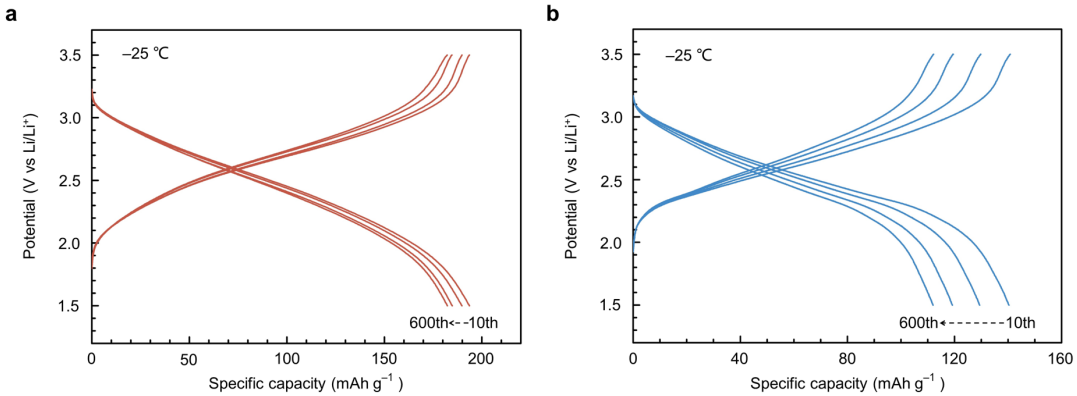

Supplementary Fig. 22 | Evaluation on the cycling performance of STTQs at low temperature.

Galvanostatic charge-discharge profiles from the 10th to 600th cycle at 0.3 A g^{-1} and −25 °C: (a) STTQ-**1** and (b) STTQ-**2**.

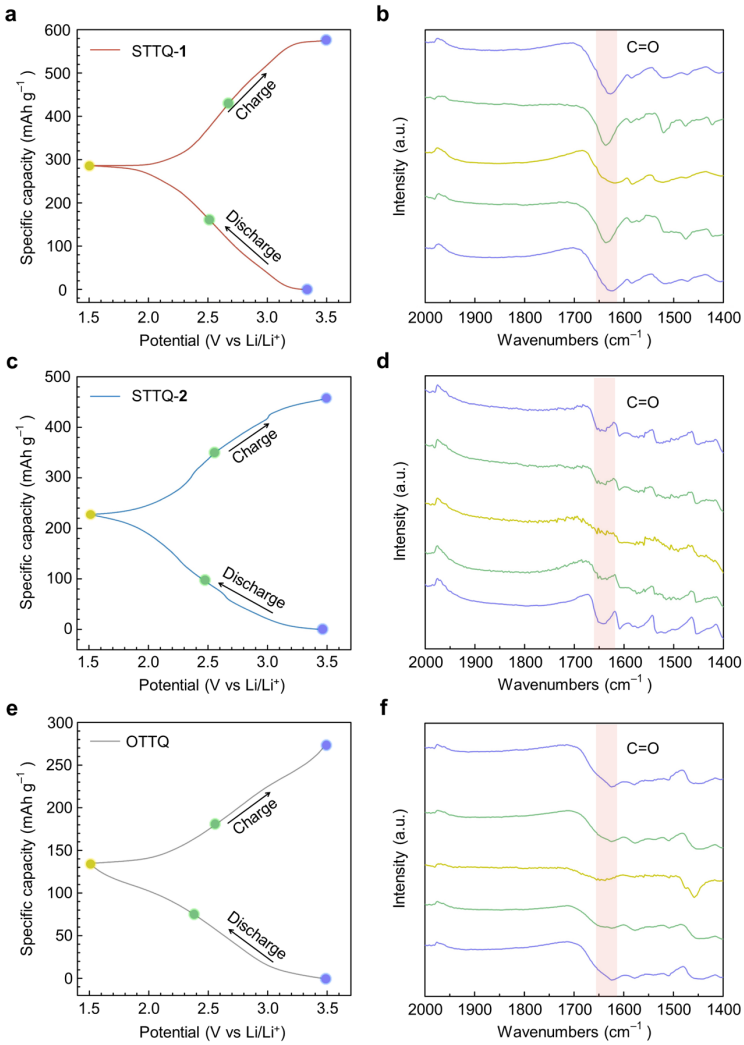

Supplementary Fig. 23 | Identification of electroactive sites in heterocyclic TTQs. Galvanostatic charge–discharge profiles (a,c,e) in a window of 1.5–3.5 V and ex-situ FT-IR spectra (b,d,f) of the cathodes obtained from the disassembled cells at different discharge and recharge states marked in a, c, and e: (a,b) STTQ-**1**, (c,d) STTQ-**2** and (e,d) OTTQ.

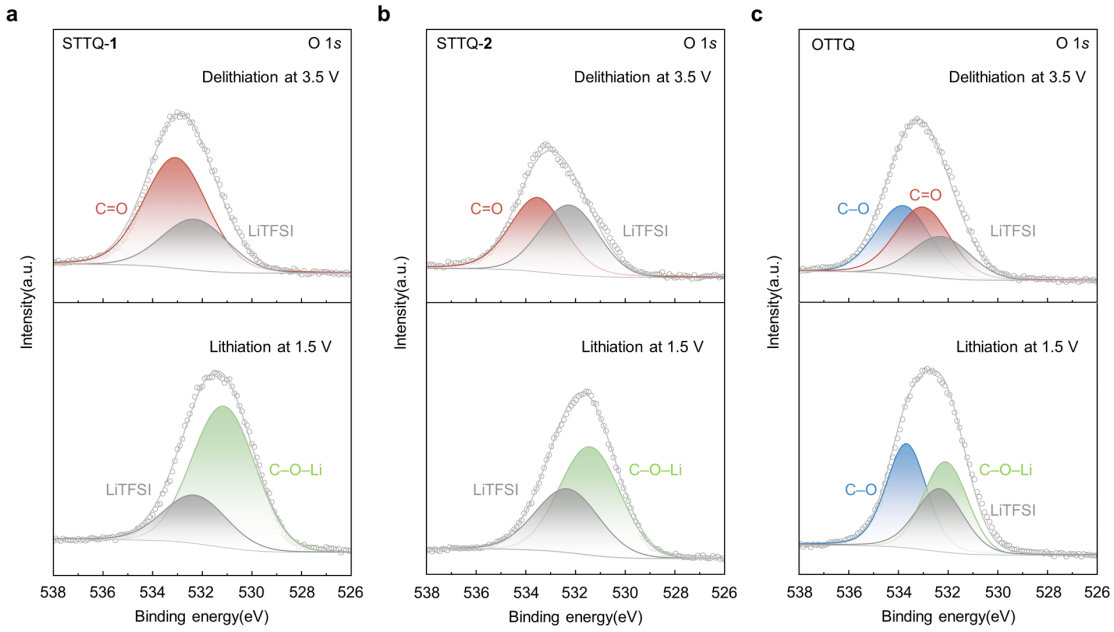

Supplementary Fig. 24 | Identification of electroactive sites in heterocyclic TTQs. High-resolution ex situ XPS spectra of O 1*s* of organic cathodes at the corresponding discharge (lithiation) and recharge (delithiation) states: (a) STTQ-**1**, (b) STTQ-**2** and (c) OTTQ.

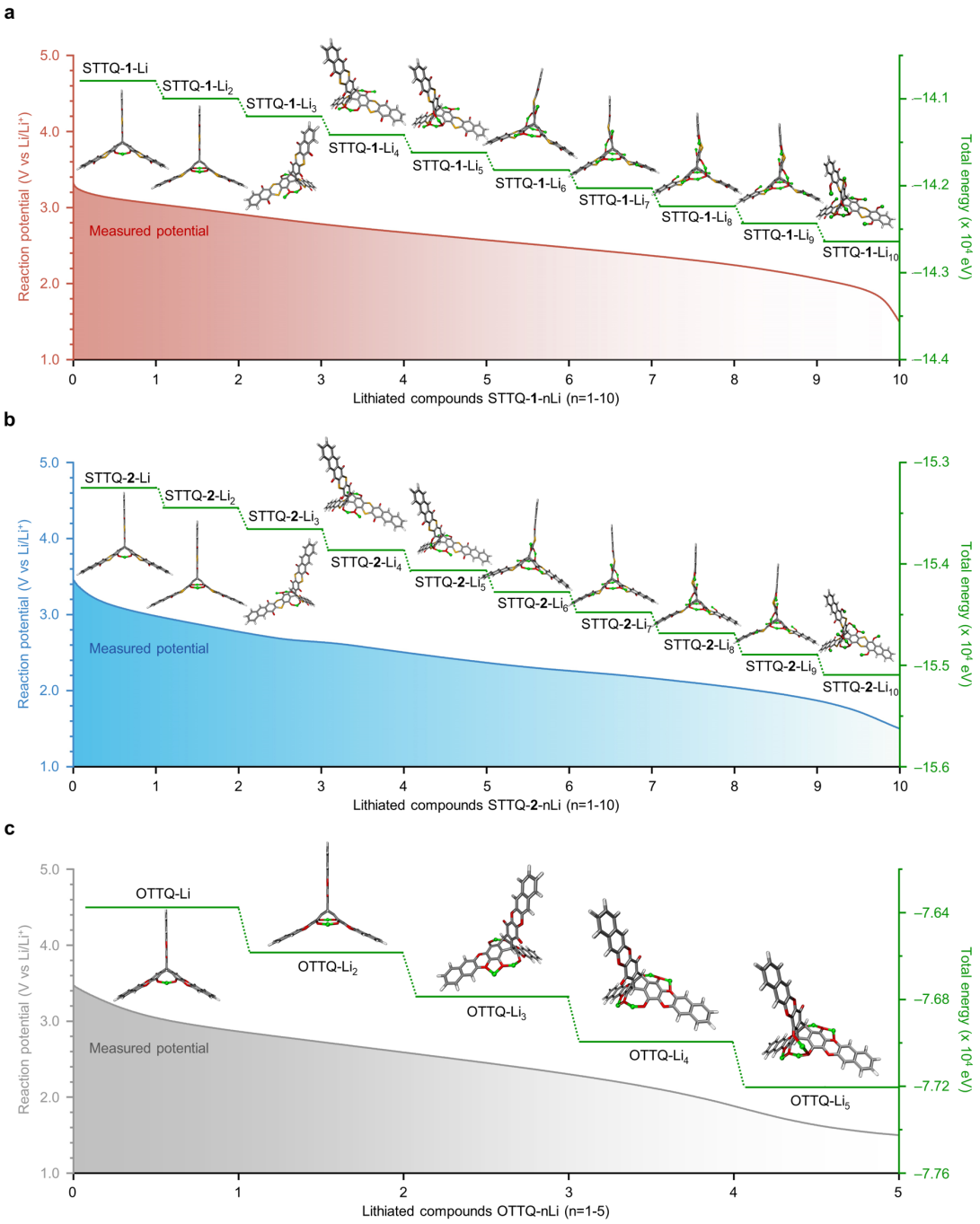

Supplementary Fig. 25 | Calculation of the lithiation pathway in heterocyclic TTQs. Reaction potentials versus Li^+/Li (STTQ-**1**: red; STTQ-**2**: blue; OTTQ: gray) and total energy of lithiated structures (eV), with green lines marking the most stable configuration at each lithiation stage: (a) STTQ-**1**, (b) STTQ-**2**, and (c) OTTQ.

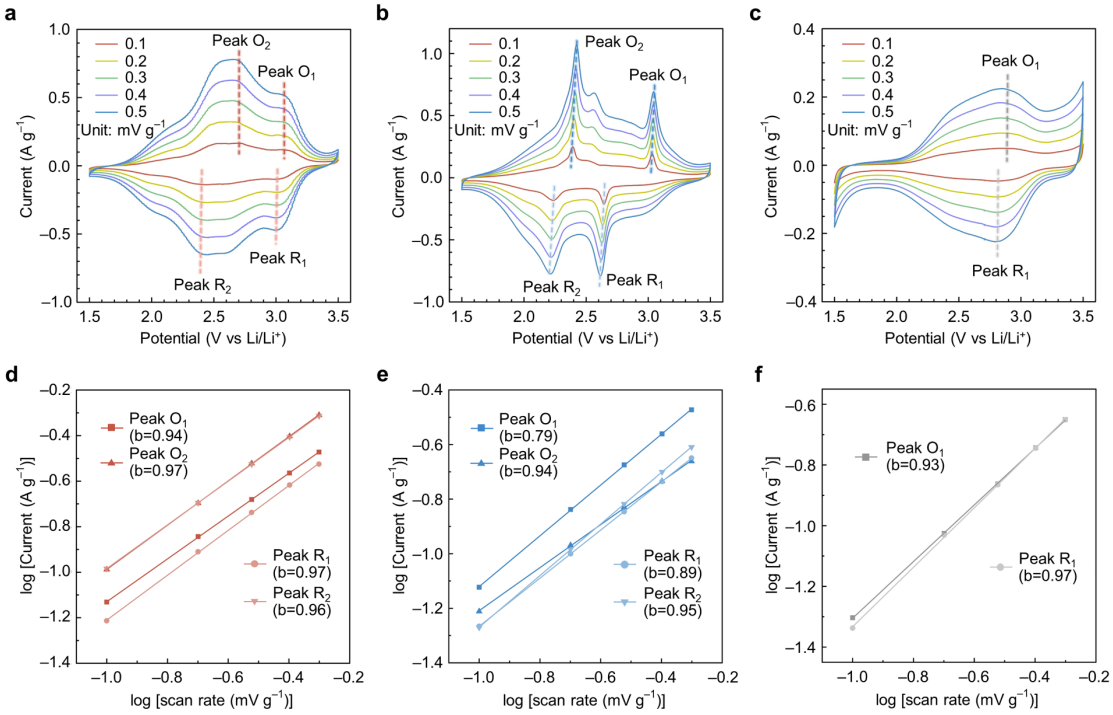

Supplementary Fig. 26 | Evaluation on the electrochemical reaction kinetics of heterocyclic TTQs.

(a–c) CV curves at varied scan rates (0.1–0.5 mV·s^{-1}) and (d–f) Linear fitting of log(i_p) vs. log(v) for redox peaks (R^2 > 0.99): (a,d) STTQ-**1**, (b,e) STTQ-**2**, and (c,f) OTTQ.

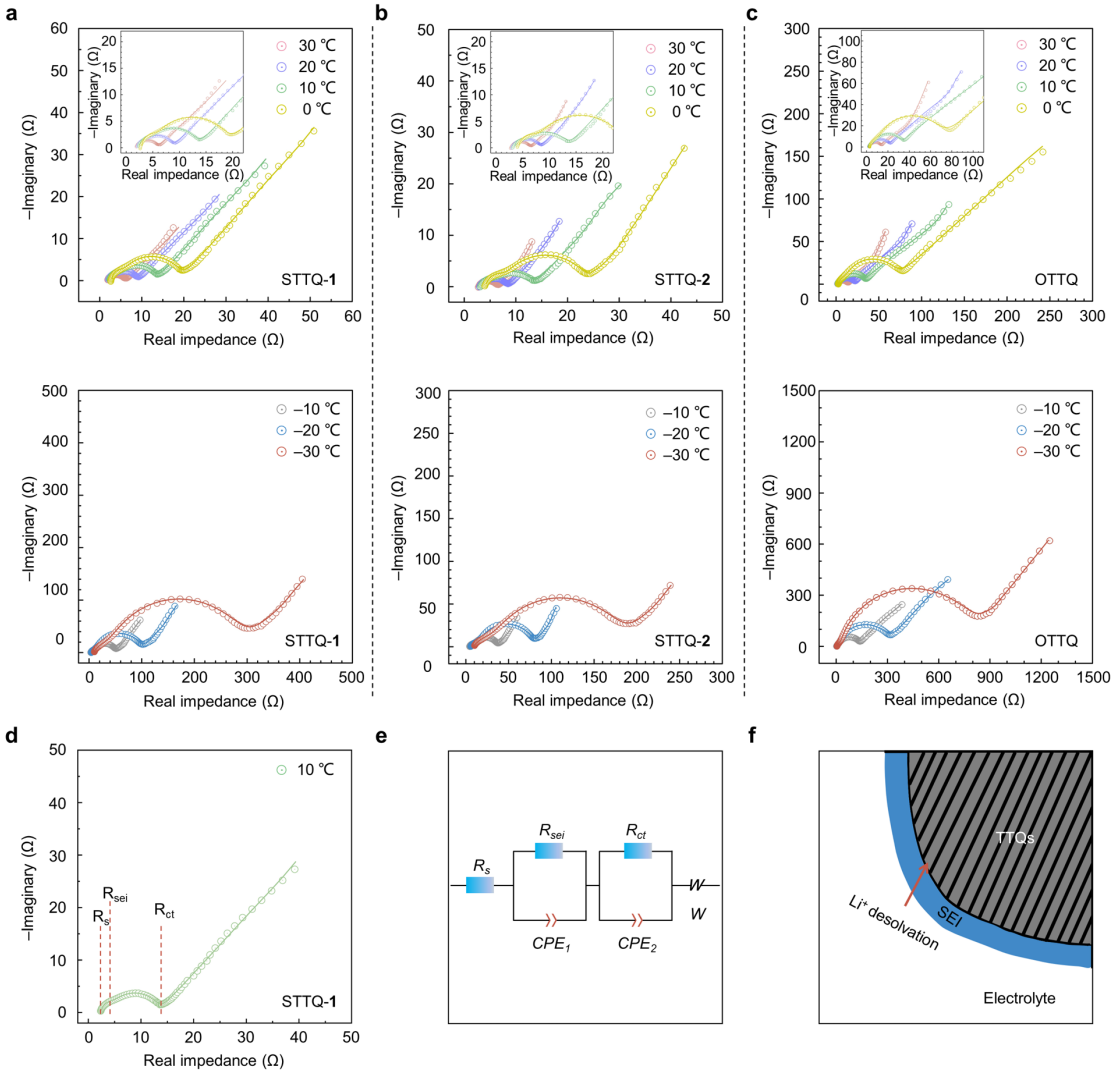

Supplementary Fig. 27 | Evaluation on the temperature-dependent charge-transfer resistance and equivalent circuit model of heterocyclic TTQs.
Nyquist plots and of EIS at different temperatures ranging from 30 to −30 °C with fitting lines (solid): (a) STTQ-**1**, (b) STTQ-**2**, and (c) OTTQ. The equivalent circuit model (e) to fit Nyquist plot of EIS (d) obtained from half cells, where R_s, R_{sei}, and R_{ct} stand for the resistance of the electrolyte, the Li^+ migration through solid-electrolyte interface (SEI) and the desolvation process (f), respectively.

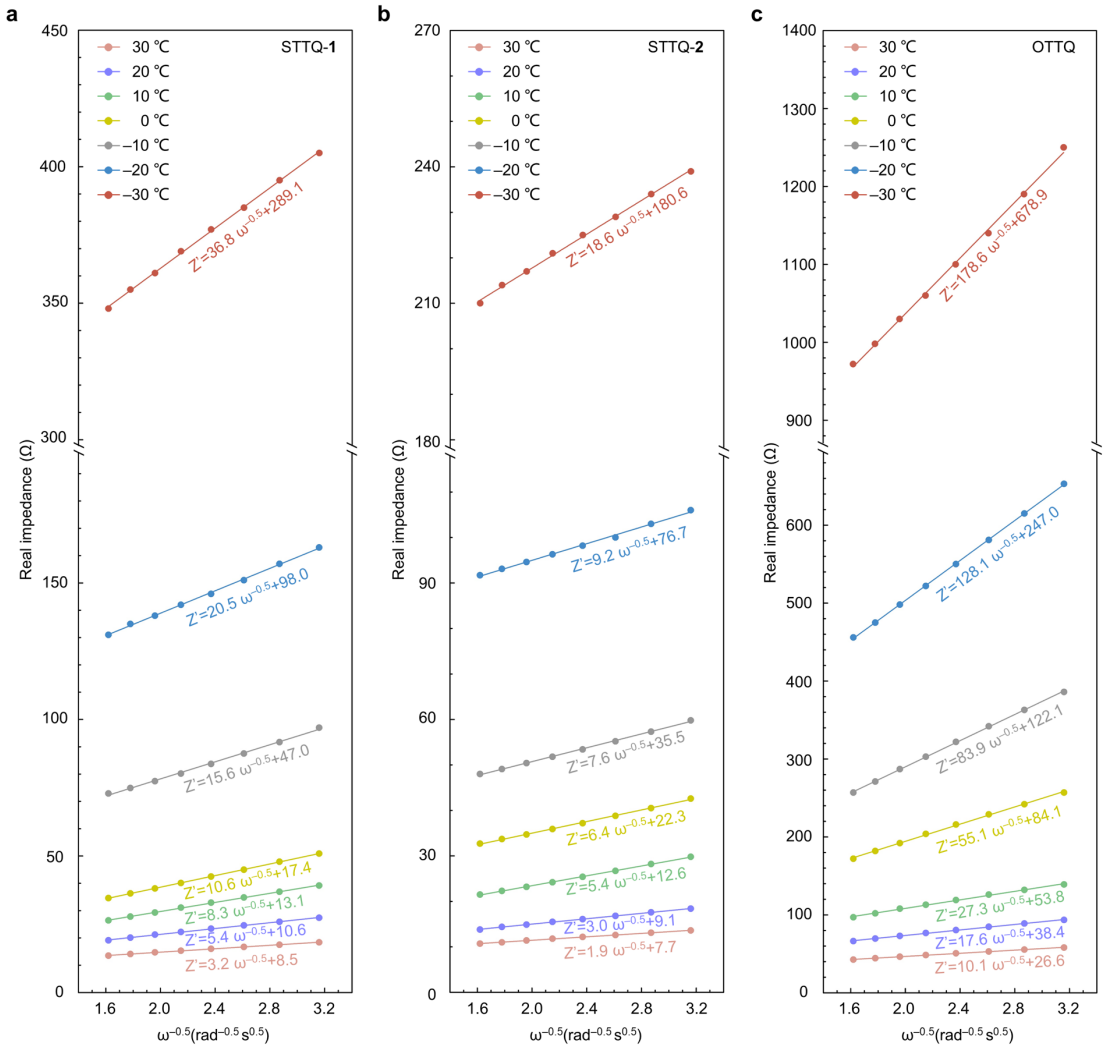

Supplementary Fig. 28 | Evaluation on the Li^+-diffusion coefficients of TTQs at different temperatures.

Linear fitting plots (R^2 > 0.99) of the real part of impedance and low frequency at different temperatures ranging from 30 to −30 °C: (a) STTQ-**1**, (b) STTQ-**2**, and (c) OTTQ.

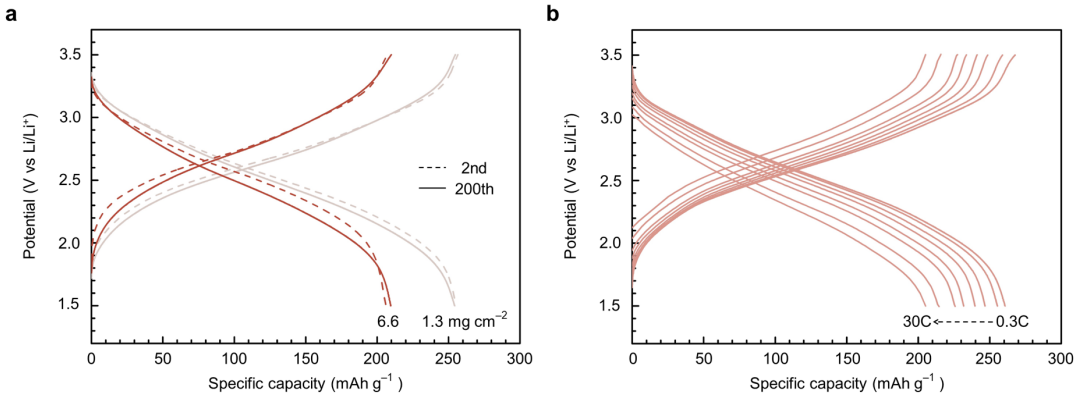

Supplementary Fig. 29 | Evaluation on the cycling and rate performance of STTQ-1 with different mass loading.

(a) Galvanostatic charge–discharge profiles from the 2nd to 200th cycle at 0.15 A g^{-1} (0.5C) with different active material mass loadings: 1.3 mg cm^{-2} (light gray), 6.6 mg cm^{-2} (red). (b) Galvanostatic charge–discharge profiles at 25 °C with active material mass loading of 2 mg cm^{-2} across rates of 0.3C to 30C.

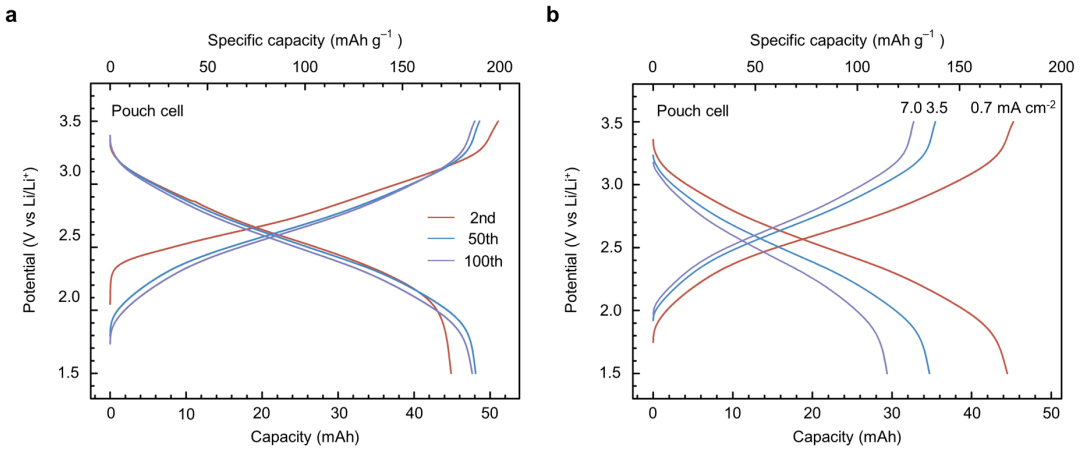

Supplementary Fig. 30 | Evaluation on the cycling and rate performance of pouch cell.

(a) Galvanostatic charge–discharge profiles from the 2nd to 100th cycle at 0.7 mA cm^{-2} with active material mass loading of 6 mg cm^{-2}. (b) Galvanostatic charge–discharge profiles at 25 °C with active material mass loading of 6 mg cm^{-2} from 0.7 mA cm^{-2} to 7 mA cm^{-2}.

3. Supplementary Tables

Supplementary Table 1 | Electrochemical performance of TTQs and the reported small molecules cathode materials

Materials	Current density (mA g^{-1})	Specific capacity (mAh g^{-1})	Average voltage (V)	Energy density (Wh kg^{-1})	Power density (W kg^{-1})	Cycle number / Capacity retention (%)	Reference
AQ	20	183	2.4	440	48	100 / 60	(1)
	200	90	2.3	207	460		
TTQ	400	250	2.6	650	1040	100 / 65	(2)
DQDPD	5000	343	2.0	686	10000	3000/82	(3)
PTO-NH_2	50	350	2.4	840	120	100 / 83	(4)
3Q	8000	147	1.8	264	14400	10000 / 65	(5)
PCT-1	500	290	2.2	638	1100	100 / 48	(6)
	2000	270	2.0	540	4000		
HATAQ	10000	209	2.2	459.8	22000	1000 / 85	(7)
TPB	47	223	2.3	513	108	100 / 91	(8)
C4Q	85	422	2.5	1055	213	100 / 89	(9)
	446	218	2.3	500	1077		
OLDT	500	272	2.3	626	1150	1000 / 76	(10)
	5000	161	2.0	322	10000		
STTQ-**1**	60	288	2.56	738	230	5000 / 79	This work
	4500	241	2.49	600	11179		
	18000	218	2.39	521	42932		
STTQ-**2**	60	239	2.46	587	216	5000 / 71	This work
	4500	203	2.35	478	10540		
	18000	180	2.24	403	40260		
OTTQ	60	135	2.41	325	216	5000 / 81.1	This work
	4500	86	2.36	203	10675		
	18000	66	2.26	149	40600		

Supplementary Table 2 | Electrochemical performance of TTQs and the reported polymeric cathode materials

Materials	Current density (mA g^{-1})	Specific capacity (mAh g^{-1})	Average voltage (V)	Energy density (Wh kg^{-1})	Power density (W kg^{-1})	Cycle number / Capacity retention (%)	Reference
PDB	20	255	2.45	624	50	1000 / 81	(11)
	1500	161	2.49	401	3346		
Li_2PDBM	50	251	1.90	477	95	2000 / 77	(12)
	2000	198	1.70	337	3400		
PIM	38	181	2.45	444	93	1400 / 99	(13)
PI	14	110	2.20	242	31	300 / 70.7	(14)
DAPQ	500	162	2.52	408	1260	3000 / 76.0	(15)
USTB	150	233	2.20	513	330	6000 / 70	(16)
	3000	187	2.14	400	6420		
BQ1	39	504	2.05	1033	79	1000 / 81	(17)
	7730	171	1.75	350	12600		
	60	288	2.56	738	230		
STTQ-**1**	4500	241	2.49	600	11179	5000 / 79	This
	18000	218	2.39	521	42932		work
	60	239	2.46	587	216		
STTQ-**2**	4500	203	2.35	478	10540	5000 / 71	This
	18000	180	2.24	403	40260		work
	60	135	2.41	325	216		
OTTQ	4500	86	2.36	203	10675	5000 / 81.1	This
	18000	66	2.26	149	40600		work

Supplementary Table 3 | Electrochemical performance of TTQs and the reported inorganic cathode materials

Materials	Current density (mA g^{-1})	Specific capacity (mAh g^{-1})	Average voltage (V)	Energy density (Wh kg^{-1})	Power density (W kg^{-1})	Cycle number / Capacity retention (%)	Reference
$LiMn_2O_4$	10	103	4.05	418	41	100 / 97	(18)
	200	94	3.85	363	770		
$LiCoO_2$	28	157	3.90	612	109	200 / 81	(19)
	420	139	3.60	500	1512		
NCM_{811}	40	187	3.84	718	154	200 / 73	(20)
	2000	85	3.34	284	6684		
$LiFePO_4$	32	159	3.34	531	107	1000 / 95	(21)
	1600	141	2.75	387	4400		
NCA	40	202	3.83	774	153	1000 / 84	(22)
TiS_2	100	205	2.14	439	214	200 / 84	(23)
STTQ-**1**	60	288	2.56	738	230	5000 / 79	This work
	4500	241	2.49	600	11179		
	18000	218	2.39	521	42932		
STTQ-**2**	60	239	2.46	587	216	5000 / 71	This work
	4500	203	2.35	478	10540		
	18000	180	2.24	403	40260		
OTTQ	60	135	2.41	325	216	5000 / 81.1	This work
	4500	86	2.36	203	10675		
	18000	66	2.26	149	40600		

Supplementary Table 4 | Low-temperature performance of TTQs and the reported cathode materials

Materials	Current density (mA g^{-1})	Temperature (°C)	Capacity (mAh g^{-1})	Capacity retention (%)	Reference
$LiNi_{1/3}Co_{1/3}Mn_{1/3}O_2$	16	−40	74	45	(24)
$LiCoO_2$	10	−50	82	60	(25)
$LiNi_{0.8}Co_{0.15}Al_{0.05}O_2$	10	−85	76	50	(26)
$Li_3V_2(PO_4)_3$	26	−30	90	80	(27)
Polyimide (PI)	36	−70	84	69	(28)
Polytriphenylamine	50	−70	69	70	(29)
CCP	100	−60	78	32	(30)
CAP	100	−60	163	70	(30)
STTQ-**1**	150	−40	191	71	This work
STTQ-**2**	150	−40	148	71	This work

Supplementary Table 5 | Li^+-diffusion coefficients (D_{Li^+}) of TTQs at different temperatures

Materials	Temperature (°C)	σ_w (Ω rad$^{0.5}$ s$^{-0.5}$)	D_{Li^+} (cm^2 s^{-1})
STTQ-**1**	30	3.2	2.90×10^{-9}
	20	5.4	9.42×10^{-10}
	10	8.3	3.61×10^{-10}
	0	10.6	2.06×10^{-10}
	−10	15.6	8.82×10^{-10}
	−20	20.5	4.74×10^{-10}
	−30	36.8	1.36×10^{-11}
STTQ-**2**	30	1.9	8.07×10^{-9}
	20	3.0	3.07×10^{-9}
	10	5.4	8.55×10^{-10}
	0	6.4	5.73×10^{-10}
	−10	7.6	3.73×10^{-10}
	−20	9.2	2.39×10^{-10}
	−30	18.6	5.34×10^{-11}
OTTQ	30	10.1	2.82×10^{-10}
	20	17.6	8.64×10^{-11}
	10	27.3	3.36×10^{-11}
	0	55.1	7.65×10^{-12}
	−10	83.9	3.07×10^{-12}
	−20	128.1	1.22×10^{-12}
	−30	178.6	5.78×10^{-13}

4. Supplementary References

1. Li, W. et al. All-solid-state secondary lithium battery using solid polymer electrolyte and anthraquinone cathode. *Solid State Ion.* **300**, 114–119 (2017).
2. Kwon, J. E. et al. Triptycene-based quinone molecules showing multi-electron redox reactions for large capacity and high energy organic cathode materials in Li-ion batteries. *J. Mater. Chem. A* **6**, 3134–3140 (2018).
3. Peng, H. et al. Boosting lithium storage performance of small-molecule organic cathodes through synergistic molecular engineering and nanostructure design. *Angew. Chem. Int. Ed.* **64**, 202502088 (2025).
4. Zheng, S. et al. Hydrogen bond networks stabilized high-capacity organic cathode for lithium-ion batteries. *Angew. Chem. Int. Ed.* **62**, 202217710 (2023).
5. Peng, C. et al. Reversible multi-electron redox chemistry of π-conjugated N-containing heteroaromatic molecule-based organic cathodes. *Nat. Energy* **2**, 17074 (2017).
6. Nakashima, K. et al. A new design strategy for redox-active molecular assemblies with crystalline porous structures for lithium-ion batteries. *Chem. Sci.* **11**, 37–43 (2020).
7. Wu, M. S. et al. Supramolecular self-assembled multi-electron-acceptor organic molecule as high-performance cathode material for Li-ion batteries. *Adv. Energy Mater.* **11**, 2100330 (2021).
8. Luo, Z., Liu, L., Zhao, Q., Li, F. & Chen, J. An insoluble benzoquinone-based organic cathode for use in rechargeable lithium-ion batteries. *Angew. Chem. Int. Ed.* **56**, 12735–12739 (2017).
9. Huang, W. et al. Quasi-Solid-state rechargeable lithium-ion batteries with a calix[4]quinone cathode and gel polymer electrolyte. *Angew. Chem. Int. Ed.* **52**, 9162–9166 (2013).
10. Shi, T. et al. Oxidized indanthrone as a cost-effective and high-performance organic cathode material for rechargeable lithium batteries. *Energy Storage Mater.* **50**, 2652–73 (2022).
11. Xie, J., Wang, Z., Xu, Z.-J. & Zhang, Q. Toward a high-performance all-plastic full

battery with a single organic polymer as both cathode and anode. *Adv. Energy Mater.* **8**, 1703509 (2018).

12. Wang, Y. et al. High-performance polymeric lithium salt electrode material from phenol–formaldehyde condensation. *ACS Appl. Mater. Interfaces* **13**, 37289–37298 (2021).
13. Wang, A. et al. Solution-processable redox-active polymers of intrinsic microporosity for electrochemical energy storage. *J. Am. Chem. Soc.* **144**, 17198–17208 (2022).
14. Wang, Z. et al. Few layer covalent organic frameworks with graphene sheets as cathode materials for lithium-ion batteries. *Nanoscale* **11**, 5330–5335 (2019).
15. Gao, H. et al. A pyrene-4,5,9,10-tetraone-based covalent organic framework delivers high specific capacity as a Li-ion positive electrode. *J. Am. Chem. Soc.* **144**, 9434–9442 (2022).
16. Liu, X. et al. In situ growth of covalent organic framework nanosheets on graphene as the cathode for long-life high-capacity lithium-ion batteries. *Adv. Mater.* **34**, 2203605 (2022).
17. Wu, M. et al. A 2D covalent organic framework as a high-performance cathode material for lithium-ion batteries. *Nano Energy* **70**, 104498 (2020).
18. Hai, Y. et al. Facile controlled synthesis of spinel $LiMn_2O_4$ porous microspheres as cathode material for lithium ion batteries. *Front. Chem.* **7**, 437 (2019).
19. Cho, J., Kim, Y. J. & Park, B. Novel $LiCoO_2$ cathode material with Al_2O_3 coating for a Li ion cell. *Chem. Mater.* **12**, 3788–3791 (2000).
20. Deng, X. et al. A comparative investigation of single crystal and polycrystalline Ni-rich NCMs as cathodes for lithium-ion batteries. *Energy Environ. Mater.* **6**, e12331 (2023).
21. Huang, X., Yao, Y., Liang, F. & Dai, Y. Concentration-controlled morphology of $LiFePO_4$ crystals with an exposed (100) facet and their enhanced performance for use in lithium-ion batteries. *J. Alloy. Compd.* **743**, 763–772 (2018).
22. Duan, J. et al. Enhanced electrochemical performance and thermal stability of $LiNi_{0.80}Co_{0.15}Al_{0.05}O_2$ via nano-sized $LiMnPO_4$ coating. *Electrochim. Acta* **221**,

14–22 (2016).

23. Mao, M. et al. Electronic conductive inorganic cathodes promising high-energy organic batteries. *Adv. Mater.* **33**, 2005781 (2021).
24. Shi, P. et al. A novel mixture of lithium bis (oxalato) borate, gamma-butyrolactone and non-flammable hydrofluoroether as a safe electrolyte for advanced lithium ion batteries. *J. Mater. Chem. A* **5**, 19982–19990 (2017).
25. Xu, J. et al. Extending the low temperature operational limit of Li-ion battery to −80 °C. *Energy Storage Mater.* **23**, 383–389 (2019).
26. Fan, X. et al. All-temperature batteries enabled by fluorinated electrolytes with non-polar solvents. *Nat. Energy* **4**, 882–890 (2019).
27. Qin, R., Wei, Y., Zhai, T. & Li, H. LISICON structured $Li_3V_2(PO_4)_3$ with high rate and ultralong life for low-temperature lithium-ion batteries. *J. Mater. Chem. A* **6**, 9737–9746 (2018).
28. Dong, X. et al. High-energy rechargeable metallic lithium battery at −70 °C enabled by a cosolvent electrolyte. *Angew. Chem. Int. Ed.* **58**, 5623–5627 (2019).
29. Dong, X., Guo, Z., Guo, Z., Wang, Y. & Xia, Y. Organic batteries operated at −70 °C. *Joule* **2**, 902–913 (2018).
30. Zheng, Y. et al. Accelerating ion dynamics under cryogenic conditions by the amorphization of crystalline cathodes. *Adv. Mater.* **33**, 2102634 (2021).